Sound absorption of plates with micro-slits backed with air cavities: Analytical estimations, numerical calculations and experimental validations

TOMASZ G. ZIELIŃSKI [(1)], FABIEN CHEVILLOTTE [(2)], ELKE DECKERS [(3,4)]

[(1)] Institute of Fundamental Technological Research of the Polish Academy of Sciences
ul. Pawińskiego 5B, 02-106 Warsaw, Poland
e-mail: tzielins@ippt.pan.pl
Corresponding author

[(2)] MATELYS – Research Lab
7 rue des Maraîchers (bâtiment B), F69120 Vaulx-en-Velin, France
e-mail: fabien.chevillotte@matelys.com

[(3)] Department of Mechanical Engineering, KU Leuven
Celestijnenlaan 300B box 2420, 3001 Heverlee (Leuven), Belgium
e-mail: elke.deckers@kuleuven.be

[(4)] DMMS Lab, Flanders Make, Belgium

Abstract

This work discusses many practical and some theoretical aspects concerning modelling and design of plates with micro-slits, involving multi-scale calculations based on microstructure. To this end, useful mathematical reductions are demonstrated, and numerical computations are compared with possible analytical estimations. The numerical and analytical approaches are used to calculate the transport parameters for complex micro-perforated (micro-slotted) plates, which allow to determine the effective properties of the equivalent fluid, so that at the macro-scale level the plate can be treated as a specific layer of acoustic fluid. In that way, the sound absorption of micro-slotted plates backed with air cavities can be determined by solving a multi-layer system of Helmholtz equations. Two such examples are presented in the paper and validated experimentally. The first plate has narrow slits precisely cut out using a traditional technique, while the second plate – with an original micro-perforated pattern – is 3D-printed.

Key words: micro-slotted plates, micro-perforated plates, sound absorption, microstructure-based modelling, 3D-printing.

1   Introduction

Microperforated panels (MPPs) and microslit absorbers (MSAs) originate from the sixties of the last century, as robust sound absorbers for harsh environments, replacing more traditional sound absorbing materials such as porous materials. Nowadays, they find many applications ranging from food courts and clean rooms for micro-electronics to launcher fairings [1]. Within these materials, the perforations are in the sub-millimeter size, ensuring energy dissipation of the sound wave into heat by mainly viscous losses; thermal losses are in general low, due to the simple pore geometries involved.

MPPs and MSAs are applied in many configurations: backed by an acoustic layer, backed by Helmholtz resonators [2], in multiple layer configurations [3], backed by porous materials [4, 5], in heterogeneous combinations of MPPs [6], etc. Usually, the perforated or micro-slotted plates in acoustic treatments can be considered as rigid, however, some applications and/or conditions require poroelastic models for perforated plates [7–9].

The well-known theory by Maa [10] allows to predict the sound absorption of a panel with circular micro-perforations considering low perforation rates. For higher perforation rates, interaction effects between the different pores have to be accounted for, e.g., see [11]. The absorption of MSAs has amongst others been studied in [12–15]. These models apply a length correction due to the flow distortion around the aperture.

MPPs or MSAs can be modelled as rigid-frame porous media. It is obvious when recalled that advanced porous models were, in fact, originally derived from the theory of sound propagation through a rigid matrix with parallel cylindrical pores normal to the surface, by introducing physically measurable microstructural parameters in order to achieve extensions to pores of arbitrary orientation and cross-section [16]. The well-established rigid-frame porous models were applied for perforated plate absorbers, e.g., in [17–19]. In this case, the micro-perforated panel is represented as a complex fluid: the complex densities accounts for the inertial and viscous losses, whereas the complex density accounts for the thermal losses. As indicated in [17], the perforation ratio can take values between 1 and 80%. However, in practice, when using simple pore geometries, it is difficult to achieve high perforation ratios. The length correction due to the flow distortion is in this case accounted for by modifying the tortuosity α_∞.

While the works mentioned above consider circular or slitted perforations, a correction factor has to be applied to account when other pore geometries are considered. For other, simple pore geometries analytical solutions can be obtained [20, 21]. Some analytical and numerical validations are given in [22]. Recently, in [23], a general formula for the length correction was proposed, shown to be valid for any shape, except for very narrow slits.

It seems that modern technologies should allow to manufacture sound absorbing porous materials of designed and possibly optimised micro-geometry [24]. However, the potential of acoustic treatments based on MPPs and MSAs seems to be still important in many applications. Moreover, Attenborough [25] has recently shown that simple slanted microslits can reproduce the behaviour of many complex microstructures.

Given the wide range of models, correction factors and lengths available in literature, the aim of this paper is to discuss many practical and some theoretical aspects concerning the modelling of plates with geometrically complex micro-slits to support their design. In this paper, a rigid frame equivalent fluid representation is used. Different practical ways to arrive at their effective properties are explained and compared, namely: (a) simple, analytical models, relying on the hydraulic radius, as well as (b) multi-scale calculations based on microstructure. Where useful, mathematical reductions are demonstrated. The different approaches are compared for two examples and validated experimentally. Guidelines to model such materials are given. The slit pattern for a thin plate in the first example was designed in order to include local elastic resonators of squared shape, although the present work is limited only to modelling of rigid plates and a consideration of elastic resonators should involve another research. The choice of perforation pattern for the second example was casual, but driven by two aims: (1) to have a non-typical pattern where slits are linked with larger openings, and (2) to allow for a quick cheap manufacturing of sample using a budget 3D-printer.

The outline of the paper is as follows. In Section 2.1 the well-established semi-phenomenological models for fluids equivalent to sound absorbing rigid porous media are briefly recalled. These models are based on the so-called transport parameters which can be determined from microstructure. The approach is discussed in Sections 2.2 and 2.3. In Section 2.2 a brief outline on numerical calculations of transport parameters is given, while Section 2.3 discusses some analytical estimations for transport parameters of micro-perforated or micro-slotted plates. In Section 2.4 a macro-scale double-layered model of a micro-slotted plate with an air cavity behind is discussed (the plate forms a thin equivalent-fluid layer coupled to a layer of air) with respect to sound absorption achieved in case of such arrangements. All of the above is demonstrated with two examples of micro-slotted plates backed with air cavities of various sizes, namely: (1) in Section 3 – a square plate with a uniform pattern of narrow micro-slits, and (2) in Section 4 – a 3D-printed disc-shape plate with separated patterns of slightly wider micro-perforations. Experimental validations with respect to the acoustic absorption coefficient are provided for both examples. Although the optimisation of perforation patterns exceeds the scope of this paper, a simple optimisation case (for slits) is briefly discussed in Section 5.

2   Modelling

2.1   Equivalent-fluid approach and semi-phenomenological models

Many sound absorbing porous materials with open porosity and sufficiently stiff skeleton (i.e., solid frame) can be modelled using the so-called equivalent-fluid approach, in which a rigid-frame porous medium is substituted by an effective fluid equivalent to it on the macroscopic level. The equivalent fluid is substantially different from the fluid in pores, even for materials with very high porosities (which is, in fact, a common feature of the majority of light sound-absorbing materials used in acoustic treatments). On the macro-scale level, the sound propagation and absorption is determined in some frequency range by solving a boundary value problem based on the Helmholtz equation defined on a domain of equivalent fluid. Such an approach is feasible for acoustic wave propagation characterised by wavelengths significantly larger than

the characteristic dimensions of micro-geometry of porous media, so that the so-called separation of scales (macro vs. micro) is valid. Provided that these three assumptions are satisfied (i.e., the open porosity, not too short waves, and motionless solid frame), the equivalent fluid models can be used for media with microgeometry of almost any shape, that is, not only foams and other cellular or skeletal materials but also fibrous or granular media with open porosity and rigid fibres or grains.

In particular, micro-slotted plates can also be treated as porous media with rigid frame. Such plates are usually made up of stiff solids (e.g., metals). On the other hand, they are usually thin which may provoke some elastic behaviour [7, 8], especially around the plate natural frequencies. It is because the efficient sound absorbing configurations consist of a micro-slotted plate (or plates) backed by an air cavity (or with air cavities between the plates). Acoustic waves penetrate such double- or multi-layer media and their energy can be dissipated not only on slits but also trapped inside the cavities. The slits in plates are narrow and usually in the form of straight channels with flat parallel walls. They can be simply small holes as in micro-porous plates often used in narrow-band mufflers or silencers operating in high temperature conditions. The slits form an open porosity pattern and (outside of the elastic plate resonances) micro-slotted plates can be modelled as other rigid porous media using the equivalent fluid approach. Thus, thin layers of effective fluids equivalent to micro-slotted plates are coupled with backing layers of air (which is also the pore-fluid since it fills the slits) and the Helmholtz problem must be solved for such multi-layer configurations.

The equivalent fluid approach is used by a family of semi-phenomenological models based on theoretical developments by Johnson *et al.* [26], Champoux and Allard [12, 19, 27], Pride *et al.* [28], and Lafarge *et al.* [29–31]. Three models are usually distinguished, namely: (1) JCA – the Johnson-Champoux-Allard model, (2) JCAL – the Johnson-Champoux-Allard-Lafarge model, (3) JCAPL – the Johnson-Champoux-Allard-Pride-Lafarge model. The JCA model requires 5 parameters (usually referred to as the transport parameters), namely: the (open) porosity ϕ, the (inertial) tortuosity α_∞, the (viscous) permeability k_0, and the viscous and thermal characteristic lengths, Λ and Λ'. JCAL and JCAPL are enhanced versions of the original JCA model and they require additional transport parameters of the porous material.

Since on the macroscopic level the Helmholtz equation is used for the domain of the effective fluid equivalent to a porous material, the effective speed of sound is required. It is in a standard way related to the corresponding effective density and bulk modulus. The effective density (or characteristic impedance) is usually also required to apply the Neumann or Robin boundary conditions. All these effective properties are complex-valued functions of frequency (to take into account the dispersion and wave attenuation in porous media).

Let f and $\omega = 2\pi f$ be the frequency and angular frequency, respectively. The frequency-dependent, complex-valued effective density $\varrho_{\mathrm{eff}}(\omega)$ is related to the real density of pore-fluid ϱ_{f} as follows:

$$\varrho_{\mathrm{eff}}(\omega) = \frac{\varrho_{\mathrm{f}} \alpha(\omega)}{\phi}, \qquad (1)$$

where ϕ is the porosity, and $\alpha(\omega)$ is the frequency-dependent and complex-valued function of dynamic viscous tortuosity. It depends on the kinematic viscosity of pore-fluid ν_{f}, as well as on some

transport parameters, namely: the porosity ϕ, the tortuosity factor α_∞, the viscous characteristic length Λ, the (static) viscous permeability k_0 (or alternatively, the static flow resistivity σ_0). In case of JCAPL model, yet another transport parameter is required, namely, the static viscous tortuosity α_0.

The frequency-dependent, complex-valued effective bulk modulus $K_{\mathrm{eff}}(\omega)$ is related to the real bulk modulus of pore-fluid $K_{\mathrm{f}} = \gamma_{\mathrm{f}} P_{\mathrm{f}}$ in the following way

$$K_{\mathrm{eff}}(\omega) = \frac{K_{\mathrm{f}}}{\phi \beta(\omega)}, \quad \text{where} \quad \beta(\omega) = \gamma_{\mathrm{f}} - \frac{\gamma_{\mathrm{f}} - 1}{\alpha'(\omega)}. \qquad (2)$$

Here: ϕ is the porosity, γ_{f} is the ratio of specific heats for the pore-fluid, P_{f} is the ambient mean pressure, and $\alpha'(\omega)$ is the frequency-dependent and complex-valued function of dynamic thermal tortuosity. This function depends of the kinematic viscosity of pore-fluid ν_{f}, and its Prandtl number N_{f}, as well as on some transport parameters, namely: on the porosity ϕ and thermal characteristic length Λ' – in case of JCA model, and additionally also on the static thermal permeability k_0' – in case of JCAL model, and yet on another parameter, namely, the static thermal tortuosity α_0' – in case of JCAPL model.

As pointed out above, the semi-phenomenological models JCA, JCAL and JCAPL provide formulas for the viscous and thermal dynamic tortuosity functions, $\alpha(\omega)$ and $\alpha'(\omega)$, respectively. These formulas (see, for example [19, 32]) are recalled in Appendix A in the form suitable for the most elaborated JCAPL model, however, they can be easily reduced to JCA or JCAL versions using model transitions discussed in Appendix B.

2.2 Numerical calculations of transport parameters

In general case of materials with open porosity, all transport parameters (for the most enhanced JCAPL model) can be determined from their microstructure by solving three uncoupled problems defined on the fluid domain of a representative porous microstructure, namely:

1. the Stokes' flow problem (the linearised steady viscous incompressible flow) – to determine the static viscous permeability and tortuosity, k_0 and α_0;

2. the Poisson problem (the re-scaled steady-state heat transfer) – to determine the static thermal permeability and tortuosity, k_0' and α_0';

3. the Laplace problem (the re-scaled electric conductivity problem) – to determine the classic (inertial) tortuosity parameter and the viscous characteristic length, α_∞ and Λ.

The porosity ϕ is known *a priori* as the main feature of micro-geometry. Also the thermal characteristic length Λ' is computed from the micro-geometry: as the doubled ratio of the volume of fluid domain to the surface of solid walls encompassing it (i.e., the doubled volume of pores to their surface).

Such microstructure-based approach for modelling of sound absorbing open-porosity media have been applied by many authors, in particular, for granular media [33–35], for (modelled in 2D) hexagonal porous structures with solid fibres (or ligaments) [36], for open-cell aluminium foams [37, 38], and more recently for

polymeric foams [39], and (ceramic) open foams with spherical pores [40]. Chevillotte et al. [41] studied a link between microstructure and acoustical macro-behavior of double porosity foams, and in [42] and [43] the microstructure-based approach was applied for 3D representations of fibrous materials. In most of these works theoretical background is recalled or more thoroughly discussed. Here, a concise theoretical discussions are presented in Appendix C and Appendix D, where also some important simplifications and reductions valid for porous media with patterns of straight flat-walled perforations are formally derived.

The micro-slotted plates can be treated as a very specific case of open-porosity media with "pores" in the shape of straight slits (channels) with flat walls parallel to the direction of viscous flow and wave propagation. These geometrical features have a strong influence for transport parameters. The theoretical derivations (see Appendix C and Appendix D) and investigations presented in this work confirmed that from solutions of the problems listed above, the following identities are observed for transport parameters: $k_0 = k'_0$, $\alpha_0 = \alpha'_0$, and $\Lambda' = \Lambda$. Moreover, the (inertial) tortuosity parameter is computed as $\alpha_\infty = 1$ (the slits are straight, *not* tortuous, and the flow distortion at inlet/outlet is neglected).

2.3 Analytical estimations of transport parameters for perforated plates

For perforated plates the porosity can be simply determined as:

$$\phi = \frac{A_s}{A_p}, \tag{3}$$

where A_s is the area of flat-walled slit or micro-pore openings, and A_p is the total area of plate.

Since the slits pass through plate as straight, narrow channels with flat parallel walls, the tortuosity α_∞ is 1 (as formally shown in Appendix D), and therefore, the thermal parameters are equal to their viscous counterparts, namely, $k'_0 = k_0$ and $\Lambda' = \Lambda$ (this will be confirmed in this work using numerical calculations). In practice, however, $\alpha_\infty = 1$ can be used only as an approximation, since for perforated plates the flow is distorted at the slit or pore opening, and usually some corrections are needed as discussed at the end of this Section. Finally, for perforated plates the permeabilities and characteristic lengths can be related to the so-called hydraulic radius R_h. In particular, both characteristic lengths are equal to it, since in general, the thermal characteristic length is defined as the doubled volume of pore-fluid to the surface of solid walls which is a generalisation of hydraulic radius.

The hydraulic radius is a measure of a channel flow efficiency, and it is a function of the shape of the channel (pipe or river, etc.) in which the fluid is flowing. It is calculated from the following formula

$$R_h = \frac{2A_s}{P_w}, \tag{4}$$

where A_s is the cross-sectional area of the flow (i.e., in the present context the area of slit, as defined above), while P_w is the so-called wetted perimeter. It is defined as the length of all border elements of the channel cross-section that are in contact with the fluid. Instead of giving a generic mathematical formula for this parameter its calculation is explained by illustrations in Figure 1.

One should be aware of the fact that some authors (see *Wikipedia* [44]) define the hydraulic radius as A_s/P_w, which would
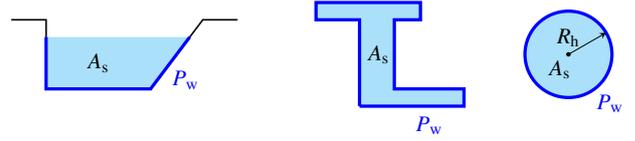

Figure 1: Wetted perimeter

mean that for a circular channel it is *not* equal to the channel radius. In the definition (4) assumed here (and by many authors, see for example [19]), this value is doubled so it *is equal* to the channel radius in the case of circular cross sections (see Figure 1), and moreover, it is now half the hydraulic diameter, i.e.: $R_h = D_h/2$; the hydraulic diameter D_h is *always* defined as $D_h = 4A_s/P_w$ [45].

Regarding what has been stated above (and also recalling some formulas from Appendix B), the following analytical estimations of transport parameters for micro-porous plates could be proposed:

$$\alpha_\infty = 1, \quad \text{or with a correction } \alpha_\infty > 1, \tag{5}$$

see formula (9) and the discussion below,

$$\Lambda = \Lambda' = R_h, \tag{6}$$

and

$$k_0 = k'_0 = \frac{\phi R_h^2}{8}, \qquad \alpha_0 = \alpha'_0 = \frac{5}{4}. \tag{7}$$

For regular perforations with identical circular holes, R_h equals to the hole radius. Notice also that when a corrected value of tortuosity is applied (i.e., $\alpha_\infty > 1$) the viscous static tortuosity $\alpha_0 = \alpha_\infty(1 + \frac{1}{4}\alpha_\infty) > \alpha'_0 = \frac{5}{4}$, see formula (B.2).

The formulas (7) for transport parameters imply that the perforated plate can be modelled as a porous medium with straight pores (channels) using the JCA model, and moreover, there are in fact only two model parameters (2 degrees of freedom), namely, ϕ and R_h.

There are, however, two drawbacks concerning these standard analytical estimations. Firstly, they are valid for typical microporous plates with circular holes or other openings of similar shape proportions. In case of plates with narrow micro-slits (instead of round perforations) the correct permeability estimations can be predicted by the following formula:

$$k_0 = k'_0 = \frac{\phi R_h^2}{12}; \quad \text{and then:} \quad \alpha_0 = \alpha'_0 = \frac{7}{6}, \tag{8}$$

which results from formula (B.3) recalled in Appendix B. For regular slit patterns (i.e., when all slits have the same width), R_h approximately equals the slit width (and $\Lambda = \Lambda' = R_h$ as before). Notice again that when a corrected value of tortuosity is applied (i.e., $\alpha_\infty > 1$) the viscous static tortuosity $\alpha_0 = \alpha_\infty(1 + \frac{1}{6}\alpha_\infty) > \alpha'_0 = \frac{7}{6}$, see formula (B.2).

The second inaccuracy arises from the distortion of the flow induced by the perforations which involves additional viscous effects at the plate surface around openings where the flow bends around. There is also another phenomenon related to the motion of air inside and directly outside of the perforation, which involves the inertial loading associated to the sound radiation at the perforation and to the distortion of the acoustic flow at the plate surface, which virtually makes the air heavier and more difficult to move inside the perforation [17]. In order to account for these phenomena, the

tortuosity of the perforated plate must be corrected according to the media in which the perforated radiates [17]. The correction can be done by introducing the correction lengths (due to the additional viscous effects and the acoustic radiation which involves the air cylinder longer than the perforation neck). Due to the low porosity of the perforated plates, this is the main parameter for modelling perforated plates. Concerning the tortuosity, we can estimate it from the sound radiation of a perforation [20].

When the medium on both sides of the perforated plate is air, the following static (i.e., frequency-independent) correction for tortuosity can be applied [17]:

$$\alpha_\infty = 1 + 2\frac{\varepsilon_c}{\ell_p}. \tag{9}$$

Here, ε_c is a correction length, while ℓ_p is the thickness of the plate. For regular circular perforations the correction length depends on the perforation radius r and the perforation rate, which is equal to the porosity ϕ. A few specific models are recalled in [17], namely, a model by Allard [12]

$$\varepsilon_c = 0.48\sqrt{\pi r^2}\left(1 - 1.14\sqrt{\phi}\right) \quad \text{for } \sqrt{\phi} < 0.4, \tag{10}$$

or a Beranek model [46]

$$\varepsilon_c = 0.48\sqrt{\pi r^2}\left(1 - 1.47\sqrt{\phi} + 0.47\sqrt{\phi^3}\right). \tag{11}$$

These models are considered as some specific or enhanced cases of models proposed by Ingard [20]. Recently, Jaouen and Chevillotte [23] have proposed a general formula for any shape (except very narrow slits):

$$\varepsilon_c = 0.82r\left(1 - 1.33\sqrt{\phi} - 0.07\sqrt{\phi^2} + 0.40\sqrt{\phi^3}\right) \tag{12}$$

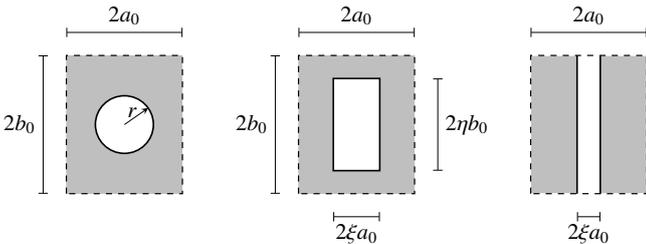where r is the radius of circular perforation or the hydraulic radius for other shapes.

Figure 2: Perforations and slits

As a matter of fact, for circular or rectangular perforations in rectangular patterns (see Figure 2), the length correction ε_c (on each side of the plate) can be found using an infinite sum of modes (see [20] and the corrected formulas in [23] and [32] where the derivations are also recalled). For rectangular perforations like in Figure 2 (middle), the length correction is given by:

$$\varepsilon_c = \sum_{m=1}^{\infty}\frac{\gamma_{m0}}{m/a_0} + \sum_{n=1}^{\infty}\frac{\gamma_{0n}}{n/b_0} + \sum_{m=1}^{\infty}\sum_{n=1}^{\infty}\frac{2\gamma_{mn}}{\sqrt{\left(m/a_0\right)^2 + \left(n/b_0\right)^2}} \tag{13}$$

where

$$\gamma_{mn} = \frac{2\xi\eta}{\pi}\left[\frac{\sin(m\pi\xi)}{m\pi\xi}\frac{\sin(n\pi\eta)}{n\pi\eta}\right]^2 \tag{14}$$

and $\xi \in (0,1)$, $\eta \in (0,1)$ (see Figure 2) are the perforation rates in the mutually orthogonal directions. (Now, they can be fairly different. Notice also that now the porosity $\phi = \xi\eta$.) Here, remember that $\lim_{x\to 0}\sin(x)/x = 1$. For long narrow slits $\eta b_0 \approx b_0$ and $\eta \approx 1$, see pattern shown in Figure 2 (right), and then

$$\varepsilon_c = \sum_{m=1}^{\infty}\frac{\gamma_{m0}}{m/a_0} = \frac{2\xi a_0}{\pi}\sum_{m=1}^{\infty}\frac{1}{m}\left[\frac{\sin(m\pi\xi)}{m\pi\xi}\right]^2. \tag{15}$$

Moreover, here again $\xi = \phi$.

2.4 Sound absorption of a plate with micro-slits backed with an air cavity

Sound absorption of (usually thin) micro-slotted or micro-porous plates makes sense only when they are parts of a larger (double or multi-layer) system. The most common, simple and quite effective solution is when a micro-porous (or micro-slotted) plate is backed with an air cavity. From the modelling perspective a double-layer system is formed, which consists of a thick backing layer of air and a much thinner layer of an effective fluid equivalent to the micro-porous plate (see Figure 3). The frequency-dependent effective properties of the fluid layer equivalent to micro-porous plate are determined in the way thoroughly discussed in previous Sections. Obviously, the shape and size of pores or slits, and the size of backing cavity ℓ_c can be adjusted in design to better confront expected noise conditions.
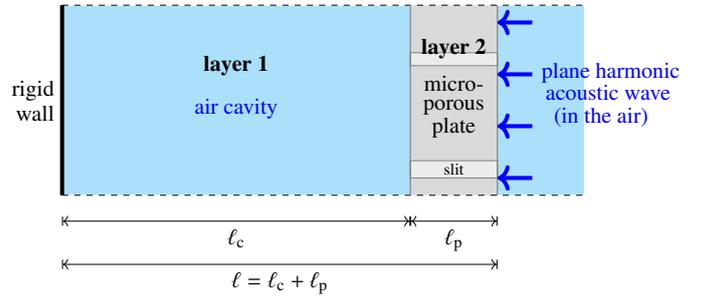

Figure 3: A double-layer configuration: a micro-slotted plate backed with an air cavity

For plane wave propagation at normal incidence, the sound absorption for a multi-layered system composed of various media is assessed in the same way as for a single material layer by determining the acoustic absorption coefficient defined as: $\mathcal{A}(\omega) = 1 - |\mathcal{R}(\omega)|^2$, where $\mathcal{R}(\omega) = \frac{Z_s(\omega)-Z_f}{Z_s(\omega)+Z_f}$ is the reflection coefficient found for the layer of material (set on a rigid wall) or the whole double-layer (as in Figure 3) or multi-layer system (in general), with $Z_s(\omega)$ being the surface acoustic impedance on the free surface (in particular, on the external surface of micro-porous plate) and Z_f the characteristic impedance of fluid adjacent to it, which obviously happens to be the same as the fluid inside slits or pores, and in cavities. The complex-valued reflection coefficient $\mathcal{R}(\omega)$ describes the ratio between the amplitudes (energies) of the outgoing reflected waves to the incident ones, so that the real-valued absorption coefficient $\mathcal{A}(\omega)$ assesses the amount of acoustic energy dissipated inside the material or multi-layered system of particular thickness ℓ.

5

The (surface) acoustic impedance $Z_s(\omega)$ – required in sound absorption calculations – is defined by the ratio of acoustic pressure to particle velocity (on a particular surface). Therefore, in general, for a multi-layered configuration of various media a coupled Helmholtz problem must be solved using, for example, the well-known Transfer Matrix Method (TMM) [47]. On the other hand, the closed analytical formulas for the acoustic pressure, velocity and (finally) impedance in such double-layer configuration as the one shown in Figure 3 can be found, for example, in [48].

3   Investigations for a square micro-slotted plate

A square plate with thickness 4 mm and a regular (3×3) array of micro-slit cells was designed and manufactured [49], see Figure 4. The micro slits inside each cell have the same pattern which forms a substructure in the plate. The shape and dimensions of micro-slit pattern are specified in Figure 4. The slit size is everywhere 0.3 mm.
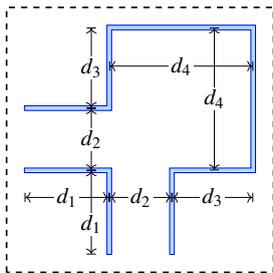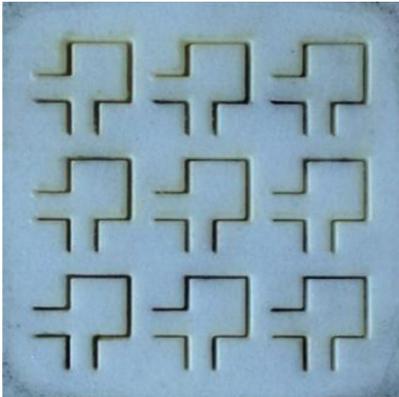
Pattern dimensions:
cell size = 11.5 mm × 11.5 mm
slit size = 0.3 mm
$d_1 = 3.60$ mm
$d_2 = 2.70$ mm
$d_3 = 3.50$ mm
$d_4 = d_2 + d_3 = 6.20$ mm

Figure 4: A square micro-slotted plate and the dimensions of slit pattern

During experimental testing the plate was set into a square impedance tube. The edge of tube's cross-section is 34.5 mm which is 3 times the size of a single micro-slit cell. The square plate is slightly larger than the size of tube's cross section, therefore, the plate edges were in fact clamped.

Table 1 shows the transport parameters determined for a single (11.5 mm × 11.5 mm) square cell with the micro-slit pattern, as shown in Figure 4. Obviously, the same transport parameters are for the whole (34.5 mm×34.5 mm) square plate since it is fully tiled with a regular dense array of identical micro-slit cells. Calculations were done analytically using the formulas for transport parameters as discussed in Section 2.3, as well as numerically using the Finite Element Method to solve the adequate boundary value problems

defined for the fluid domain of a single micro-slit cell. The numerical calculations were carried out for three problems (the Stokes flow, the Laplace problem, and the Poisson), however, as expected, the results for viscous and thermal permeabilities were numerically the same, although the viscous permeability was computed from the solution of Stokes' flow, whereas the thermal one was determined from the solution of Poisson problem. The same can be said about the static viscous and thermal tortuosities, namely, the same results are obtained from the steady viscous flow described by the Stokes' equation, as from the re-scaled thermal problem described by the Poisson's equation. The tortuosity parameter determined numerically from the solution of Laplace problem was 1.00 and the viscous characteristic length was equal to the thermal characteristic length computed as the double ratio of the total volume of slit to the surface of slit walls. Therefore, in fact only the Poisson problem needs to be solved (in order to determine the permeabilities and static tortuosities), since the porosity and characteristic lengths are determined directly from the micro-geometry, and the (inertial) tortuosity is 1. On the other hand, the analytical estimations involved also the tortuosity correction, so that $\alpha_\infty > 1$. Two analytical estimations are compared: the one using formulas (7) ideal for circular perforations, and the other using formulas for narrow slits (8). The corrected tortuosity was in both cases computed using formula (9), however, in the first case, the length correction was estimated as (12) with $r = R_h$, and in the second case, the estimation (15) was used with $\xi = \phi$ and $2a_0 = R_h$.

Table 1 compares the results of numerical calculations with the analytical approximations. In case of the investigated square plate, there is some noticeable difference in the numerical and analytical results for permeabilities when the formula for round (circular) perforations is used, while as expected, the formula for slits gives a prediction close to the numerical result. The analytical (inertial) tortuosity corrections entails also a significant increase in values of the static viscous tortuosity, while the static thermal tortuosity remains unaffected. The numerical result for the static (viscous or thermal) tortuosity is somehow in between the analytical estimations of static thermal tortuosity for slits and circular perforations, namely: $\frac{7}{6} < 1.212 < \frac{5}{4}$.

The transport parameters – obtained from two analytical estimations and the numerical calculations – were used to determine the effective properties of the equivalent fluid. Then, the acoustic absorption of the micro-slotted plate backed with an air cavity was computed for two cavity sizes, namely: 30 mm and 53 mm. Figure 5 compares these results with measurements done in the impedance tube. The following is observed:

- the standard analytical estimation (which is the one assuming circular perforations and without the tortuosity correction, i.e., $\alpha_\infty = 1$ and $\alpha_0 = \alpha_0' = \frac{5}{4}$) is significantly worse than other results;

- the numerical results are quite accurate (i.e., with only small discrepancies from the experimental curves) and they are almost the same as the analytical estimations for slits without the tortuosity corrections (i.e., when $\alpha_\infty = 1$ and $\alpha_0 = \alpha_0' = \frac{7}{6}$);

- a slight improvement is still gained when the tortuosity correction is also applied (i.e., for $\alpha_\infty = 1.105$ and $\alpha_0 = 1.308$);

Table 1: Transport parameters for the micro-slit cell: analytical estimations and numerical calculations using the Finite Element Method

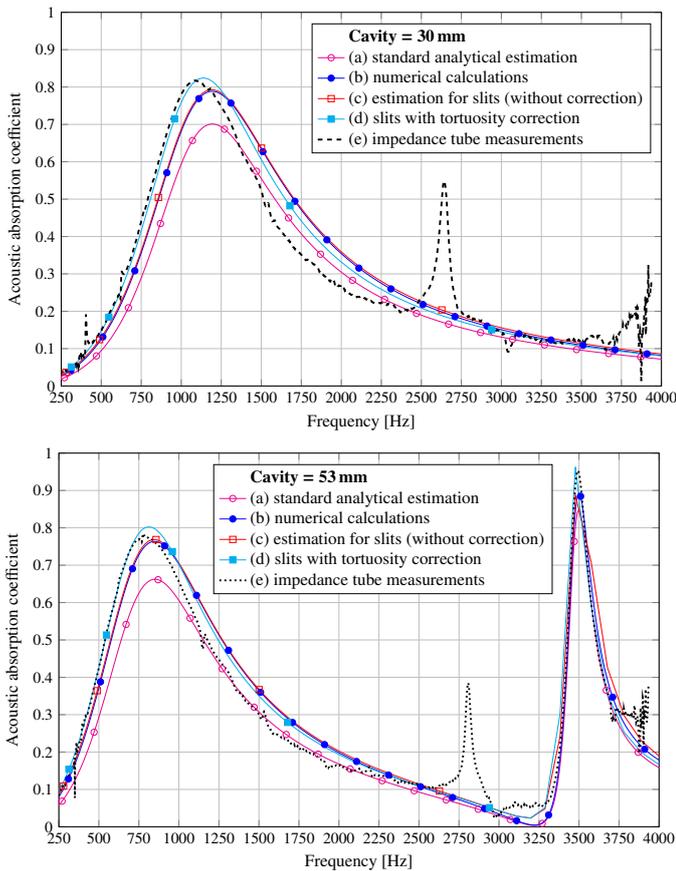| Transport parameters | | | Analytical estimations | | Numerical |
Parameter	Symbol	Unit	for circles	for slits	calculations
porosity	ϕ	%	7.667	7.667	7.667
permeabilities	$k_0 = k_0'$	$10^{-10}\,\mathrm{m}^2$	8.340	5.552	5.751
inertial tortuosity	α_∞	–	1.077	1.105	1.00
static viscous tortuosity	α_0	–	1.367	1.308	1.212
static thermal tortuosity	α_0'	–	1.25	1.167	1.212
characteristic lengths	$\Lambda = \Lambda'$	mm	0.295	0.295	0.295

Figure 5: Acoustic absorption for the square plate with micro slits backed with an air cavity (30 mm or 53 mm thick): measurements and the results based on the analytical estimations and numerical calculations of transport parameters

- the cavity resonance at 3.5 kHz (for the case of larger air cavity) is very well represented in the model;

- the experimental resonances at about 2.7 kHz (smaller air cavity) or 2.8 kHz (larger air cavity) are related to elastic behaviour of square plate, and therefore, they are not present in the model.

4 Investigations for a circular micro-perforated plate

4.1 Circular plate design

A CAD model of a circular plate with diameter 63.5 mm and thickness 12 mm was created with a pattern of micro-slits in the form of

"IPPT" acronym as shown in Figures 6 and 7. The main width of slits was designed as $a = 1$ mm, however, in some places it is doubled, namely $b = 2a$ (see Figure 6). The "IPPT" pattern of slits is set into a rectangular cell with dimensions $d_1 \times d_2$, where $d_1 = 21$ mm and $d_2 = 15$ mm, and the other distances are: $d_3 = 3$ mm, $d_4 = 3.5$ mm, and $d_5 = 4$ mm (see Figure 6). A (4×3) array of such cells was set onto the circular disk of plate, so there are 12 "IPPT" slit patterns, however, the 4 of them at corners are only partial since they cross the disk border (see Figure 7). This is important to observe, since – because of that feature – the porosity of circular plate would differ slightly from the porosity of the rectangular cell.

The CAD model was used to 3D-print the disk of micro-slotted plate using the Zortrax M200 printer, see Figure 7. The 3D-printed specimen was examined under a microscope. Apart form a rough surface and other imperfections, it was found that the actual slit
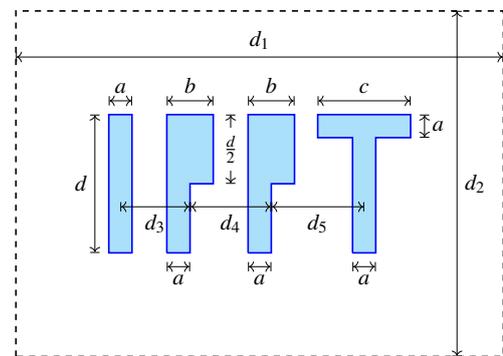

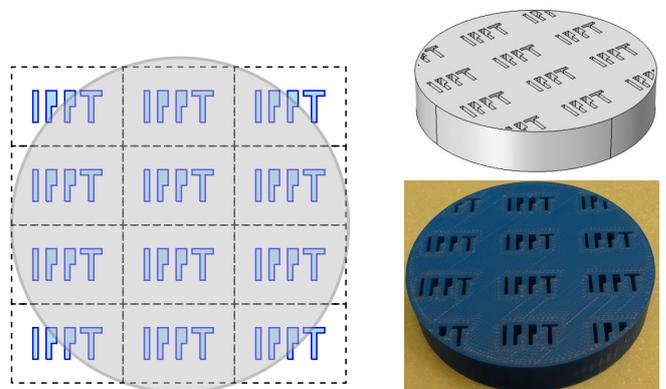**Figure 6:** A pattern of slits in the shape of "IPPT" acronym inside a rectangular cell

Figure 7: A (4×3) array of the "IPPT" slit-pattern cells on the circular disk, the corresponding designed CAD model and the 3D-printed circular disk with micro-slits in the shape of "IPPT" acronym
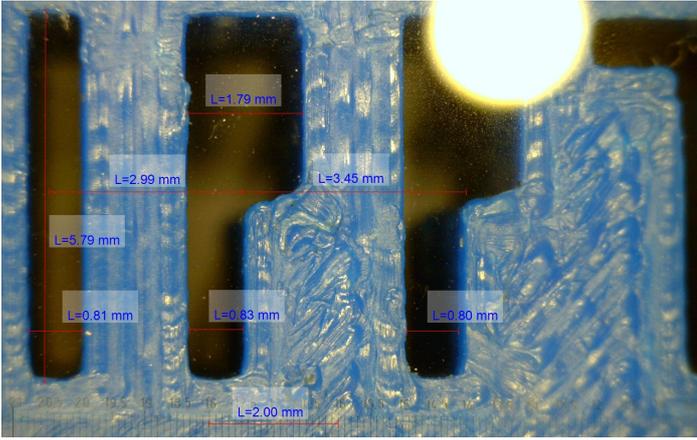
Figure 8: A zoomed fragment of a microscope photo of the "IPPT" slits with a calibration glass (with the scale resolution of 0.1 mm) set on the surface of the disk (here, all marked lengths "L" are assigned their actual values after the calibration)

Table 2: Designed and corrected ($\sim$ actual) values of slit dimensions (see Figure 6)

Slit dimensions	
(A) designed values	**(B)** corrected values
$a = 1\,\text{mm}$	$a' = a - \Delta = 0.8\,\text{mm}$
$b = 2\,a = 2\,\text{mm}$	$b' = b - \Delta = 1.8\,\text{mm}$
$c = 4\,a = 4\,\text{mm}$	$c' = c - \Delta = 3.8\,\text{mm}$
$d = 6\,a = 6\,\text{mm}$	$d' = d - \Delta = 5.8\,\text{mm}$

(correction: $\Delta = 0.2\,\text{mm}$)

widths are narrower (by approximately 0.2 mm) than the designed values, see Figure 8. The microscope examination allowed to propose systematic corrections for some dimensions of the "IPPT" pattern of slits; the corrected values and the original designed values are given in Table 2.

4.2 Transport parameters

The transport parameters were calculated analytically, using formulas (7) or alternatively (8), and numerically as described in Section 2.2, Appendix C and Appendix D – for both cases of perforation size, namely: (A) for the original designed values, and (B) the corrected ones (see Table 2). The analytical estimations were based on the exact porosity and hydraulic radius, both of which were determined from the whole perforation pattern, since the four of nine IPPT-shape perforations (see Figure 7) are cut by the disc border. To compute them, the wetted perimeter and the total area of perforation (slits) were found (for both cases) as: (A) $P_\text{w} = 674\,\text{mm}$, $A_\text{s} = 3.309 \times 10^{-4}\,\text{m}^2$, respectively, and (B) $P_\text{w} = 640\,\text{mm}$, $A_\text{s} = 2.685 \times 10^{-4}\,\text{m}^2$, respectively. The porosity ϕ and hydraulic radius R_h are listed in Table 3 together with the remaining transport parameters (notice that the hydraulic radius is the same as characteristic lengths, $R_\text{h} = \Lambda = \Lambda'$). These analytical estimations involved corrections for tortuosity, using formula (9), where the correction length was computed as (12) with $r = R_\text{h}$, and alternatively, as (15) for narrow slits (with $\xi = \phi$ and $2a_0 = R_\text{h}$), which entailed also corrections for the static viscous tortuosity. The permeabilities were also computed from two alternative formulas: as for circular perforations (7), and for narrow slits (8). In Table 3 the results of numerical calculations are also presented. Since in cir-
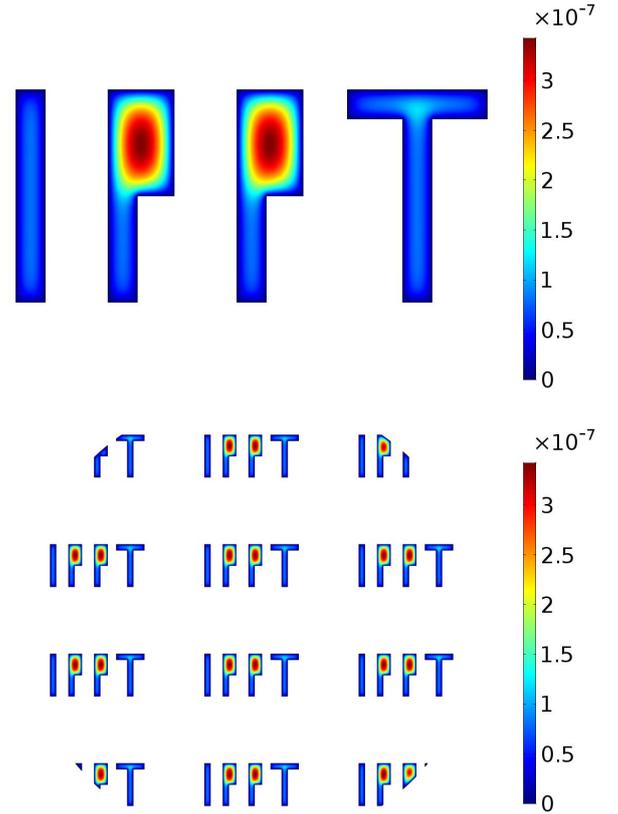

Figure 9: Microscale fields re-scaled to the unit of permeability $[\text{m}^2]$ for the single-cell calculations (top) and for the whole circular perforated plate (bottom).

cular plate some of the cells are cut by the circular border (see Figure 7), the transport parameters were obtained from the numerical solution of the Poisson problem defined on the *whole* perforation – see Figure 9 (bottom) – rather than on a single perforated cell – see Figure 9 (top) – which in fact would give only slightly different values. From the comparison between the numerical results and analytical estimations, one can observe that permeabilities are better estimated when the formula for circular perforations, $\phi R_\text{h}^2 / 8$, is used. Another observation is that the numerically-determined static tortuosities are much higher than their analytical estimations – even in case of the viscous tortuosities which were analytically increased using the corrected lengths. This would perhaps compensate for the lack of correction in the numerically-determined inertial tortuosity (which equals 1).

As observed above, the permeability estimation for narrow slits does not work correctly for the IPPT plate: the correct permeability is much higher. This is because the IPPT perforation pattern is far from the narrow slits: there are in fact two, extremely different, slit or perforation widths ($a' = 0.8\,\text{mm}$ and $b' = 1.8\,\text{mm}$), and the slits are proportionally wide (*not* narrow) since they are relatively short and based on rectangular shapes. Below, a discussion concerning the correct permeability estimation for a single rectangular perforation is given. It will be shown that this value can be even larger than the estimation for circular perforations with the same hydraulic radii. (Notice that the edge-length of a square perforation with the same hydraulic radius as a circular perforation is equal to the circle diameter, so that the square perforation permeability must be higher, even if the porosities are set equally.) Nev-

Table 3: Transport parameters for IPPT-plate – for two cases of slit-size, (A) and (B), see Table 2 – numerical results and analytical estimations (for circular perforations and narrow slits)

Transport parameters			Analytical estimations				Numerical	
Parameter	Symbol	Unit	for circles		for slits		calculations	
porosity	ϕ	%	10.45	8.478	10.45	8.478	10.45	8.478
permeabilities	$k_0 = k_0'$	$10^{-9}\,\mathrm{m}^2$	12.59	7.456	8.393	4.971	12.91	8.193
inertial tortuosity	α_∞	–	1.077	1.071	1.100	1.095	1.00	1.00
static viscous tortuosity	α_0	–	1.367	1.357	1.302	1.294	1.644	1.810
static thermal tortuosity	α_0'	–	1.25	1.25	1.167	1.167	1.644	1.810
characteristic lengths	$\Lambda = \Lambda'$	mm	0.982	0.839	0.982	0.839	0.982	0.839
			(A)	**(B)**	**(A)**	**(B)**	**(A)**	**(B)**

ertheless, for complex perforation patterns numerical calculations seems to be necessary.

Let us consider a single rectangular perforation with dimensions d_x and $d_y = \zeta\, d_x$, so that the proportion coefficient is $\zeta = d_y/d_x$, and the rectangle width is: $\min(d_x, d_y) = d_x \min(1, \zeta)$. For such a rectangular aperture the hydraulic radius is $R_\mathrm{h} = d_x \zeta/(\zeta + 1)$, which means that for $\zeta \gg 1$: $R_\mathrm{h} \approx d_x$ (as a matter of fact, $R_\mathrm{h} \to \min(d_x, d_y)$ for $\zeta \to \infty$ or $\zeta \to 0$, that is, when the rectangular perforation becomes a narrow slit). The permeabilities $k_0 = k_0'$ and hydraulic radii R_h were computed numerically for such single rectangular perforations of various proportions ζ, in order to determine the correct values of the denominator $\mathcal{D}$ in the estimation formula

$$k_0 = \frac{\phi R_\mathrm{h}^2}{\mathcal{D}}. \tag{16}$$

Remember that $\mathcal{D} = 8$ exactly for any circular perforation. This value will vary for rectangular perforations. Figure 10 presents the actual values of the denominator $\mathcal{D} = \phi R_\mathrm{h}^2/k_0$ with respect to the rectangle proportion coefficient ζ and to the ratio $\chi = R_\mathrm{h}/\min(d_x, d_y)$ of the hydraulic radius and the rectangle width. The corresponding proportions of a series of rectangles are also depicted. It was confirmed that for narrow slits (i.e., for $\zeta \to \infty$ or $\zeta \to 0$, and $\chi \to 1$) the denominator $\mathcal{D} \to 12$. On the other hand, $\mathcal{D}$ drops nearly to 7 for the square perforations (i.e., for $\zeta = 1$, $\chi = 0.5$). Finally, the rectangle proportion $\zeta \approx 2.27$ (or $\zeta \approx 1/2.27 \approx 0.44$; for both $\chi \approx 0.694$) was found when required that $\mathcal{D} = 8$, which is the exact value of the denominator for a circular perforation. (In Figure 10: $\kappa = \phi k_3(x_1, x_2)/k_0 = \phi k'(x_1, x_2)/k_0'$, see Appendix C.)

4.3 Sound absorption

The frequency-dependent effective properties (density, bulk modulus, speed of sound) of a fluid layer equivalent to the micro-slotted plate characterised by the transport parameters determined above (numerically or analytically) were computed for all the considered cases and ways of calculation, using formulas recalled in Section 2.1 and Appendix A, and the properties for air in slits taken for the ambient conditions of temperature and pressure determined during the experimental testing, namely, for 22°C and 1005 hPa (that is, the air density $\varrho_\mathrm{f} = 1.19\,\mathrm{kg/m^3}$, the kinematic viscosity $\nu_\mathrm{f} = 1.55\,\mathrm{m^2/s}$, the Prandtl number $N_\mathrm{f} = 0.71$, the specific heat ratio $\gamma_\mathrm{f} = 1.40$, and the adiabatic bulk modulus $K_\mathrm{f} = 141\,\mathrm{kPa}$). Obviously, the same air properties (i.e., the density and bulk modulus) were applied for the air in cavities (of various sizes) when
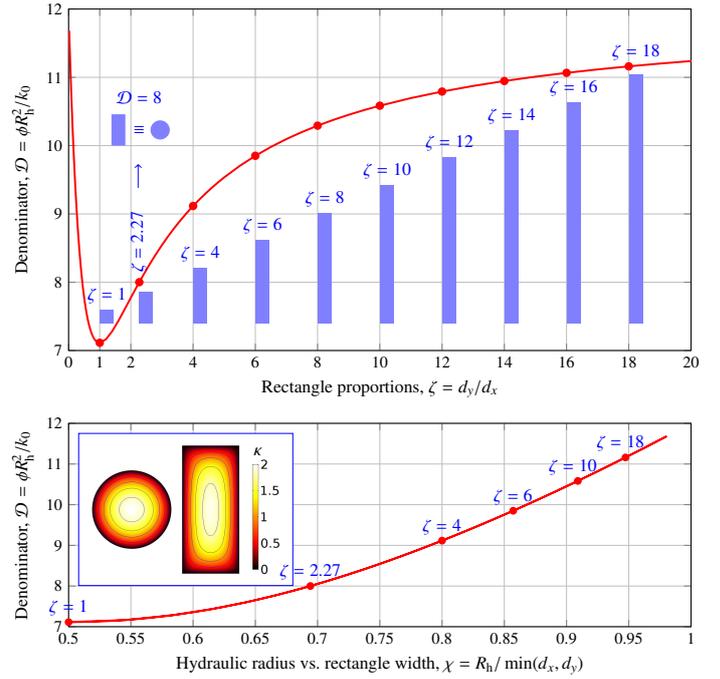

Figure 10: The exact value of the denominator $\mathcal{D}$ in the formula $k_0 = \phi R_\mathrm{h}^2/\mathcal{D}$ for the permeability of a single rectangular perforation, with respect to the rectangle proportions or the ratio of the hydraulic radius to the rectangle width

solving the double-layered problems of sound absorption of a perforated plate backed by an air cavity, as described in Section 2.4. Although, these macroscopic double-layered problems are solved analytically (see, for example [48]), some of the results presented below are denoted as *numerical* – when they are based on the numerically-determined transport parameters.

Sound absorption was measured (at 22°C and 1005 hPa) in the circular impedance tube for both sides of the disk-shape micro-slotted plate (see Figure 11) backed by air cavities of various sizes.
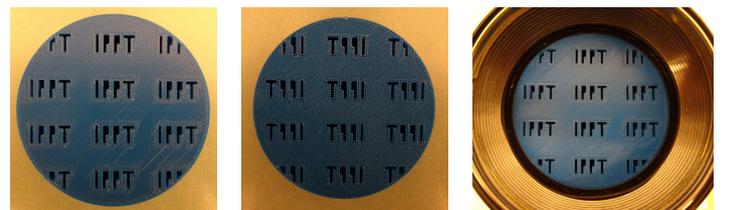

Figure 11: Both sides of the circular disk (with "IPPT" slits) and the disk inside an impedance tube
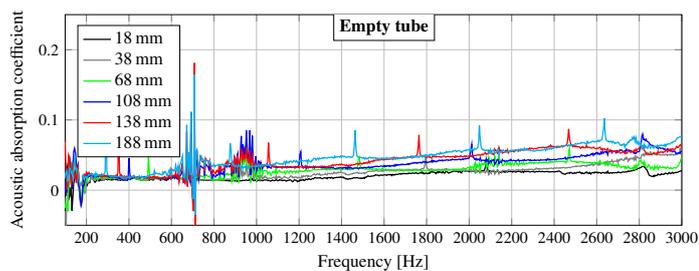
Figure 12: Acoustic absorption for various air cavities (empty tube, without the plate) coming from some non-negligible losses on the walls of the circular impedance tube of diameter 63.5 mm

The total thickness of the 12 mm-thick plate plus air cavities varied from 3 cm to 20 cm. The corresponding measurements carried out for both sides of the plate were practically the same (and an average is presented in graphs below). It was found that there are some small but perhaps *non* negligible losses on the walls on the circular impedance tube which result in some acoustic absorption in the empty tube, that is, for air cavities without the plate. This absorption is generally higher for larger cavities and it increases with frequency exceeding 0.05 in higher frequency ranges, see Figure 12. These results were appropriately used (as some kind of a background noise) to modify slightly the original measurements of the plate backed by air cavities.

The experimental curves of acoustic absorption coefficient are compared in Figures 13–18 with some modelling results, namely, the numerical ones obtained for the designed (A) and corrected micro-geometry (B), and the analytical estimations which for the sake of clarity are presented only for the corrected micro-geometry (B), but for two kinds of the perforation shape, i.e, circular pores or narrow slits. An obvious observation is that the modelling results for the original (designed) micro-geometry, i.e, for the case (A), differ much more from the measurements than the results obtained for the corrected (actual) micro-geometry, i.e., for the case (B). It was also checked that the analytical estimations without any tortuosity corrections (not presented in the graphs) were also not accurate. When the analytical correction for tortuosity is applied the estimations of sound absorption tend to be quite correct. The absorption estimations based on the formula for
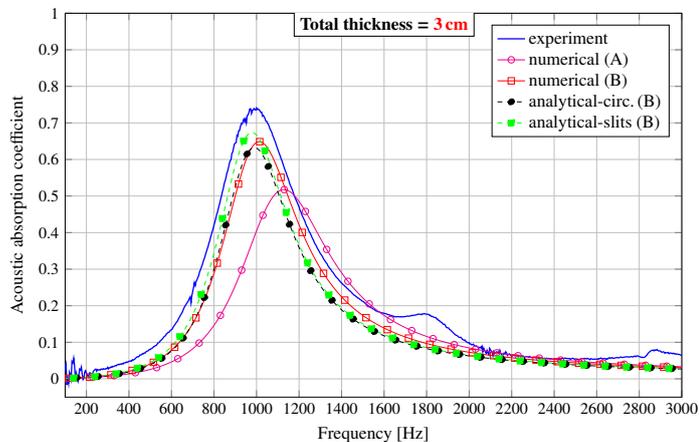

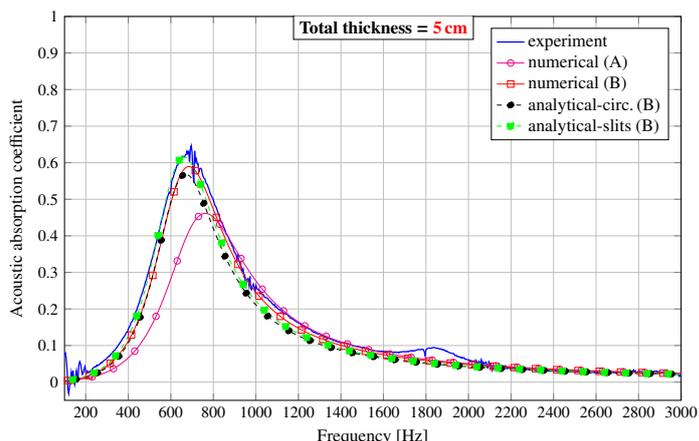**Figure 13:** Acoustic absorption for the circular micro-perforated plate backed with an air cavity of $(3\,\text{cm} - 12\,\text{mm}) = 18\,\text{mm}$

Figure 14: Acoustic absorption for the circular micro-perforated plate backed with an air cavity of $(5\,\text{cm} - 12\,\text{mm}) = 38\,\text{mm}$
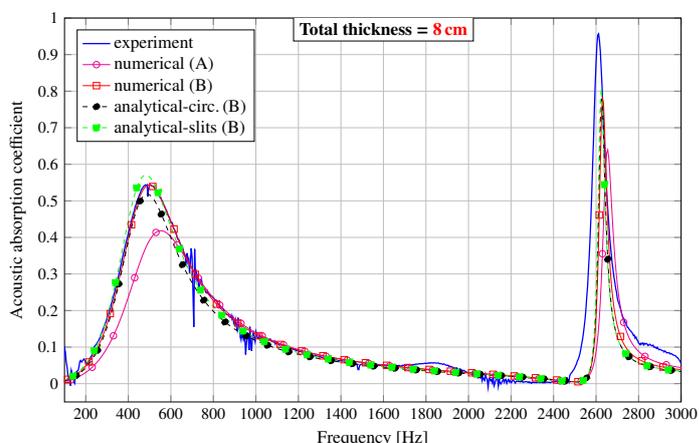
Figure 15: Acoustic absorption for the circular micro-perforated plate backed with an air cavity of $(8\,\text{cm} - 12\,\text{mm}) = 68\,\text{mm}$
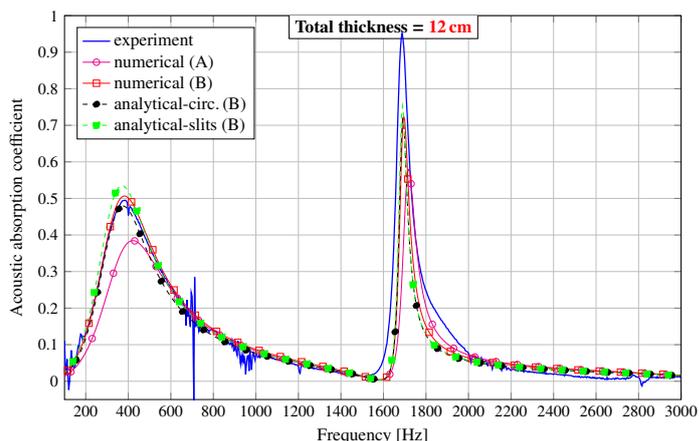
Figure 16: Acoustic absorption for the circular micro-perforated plate backed with an air cavity of $(12\,\text{cm} - 12\,\text{mm}) = 108\,\text{mm}$

permeability for circular perforations are more similar to the corresponding numerical results; the differences are not large and in some cases (namely, for small air cavities) less significant than the discrepancies to the experimental results. The numerical results for the case (B), i.e., the actual micro-geometry, agree rather well with the experimental curves thanks to the accurately determined

Figure 17: Acoustic absorption for the circular micro-perforated plate backed with an air cavity of $(15\,\text{cm} - 12\,\text{mm}) = 138\,\text{mm}$

Figure 18: Acoustic absorption for the circular micro-perforated plate backed with an air cavity of $(20\,\text{cm} - 12\,\text{mm}) = 188\,\text{mm}$
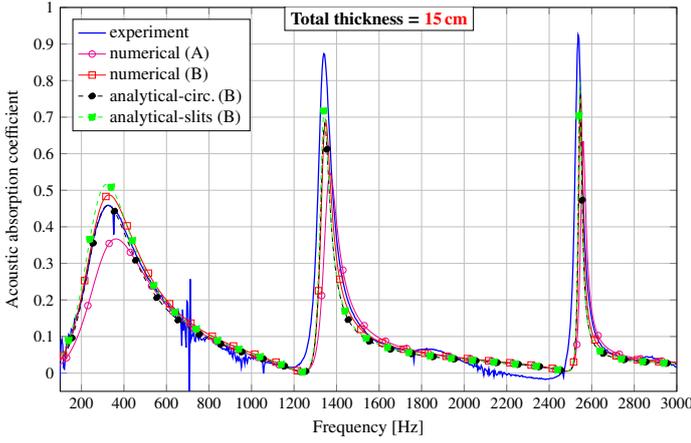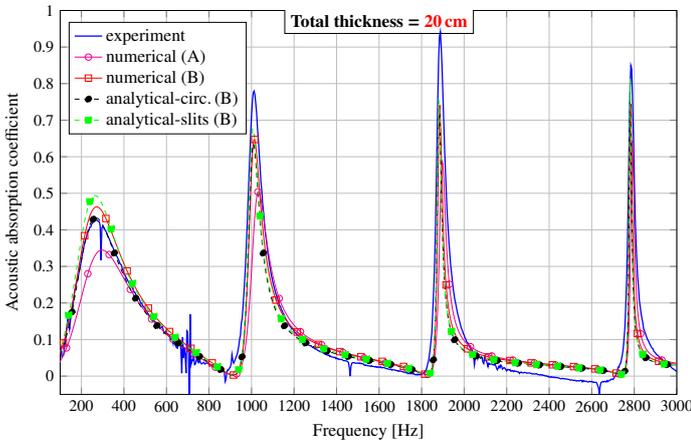
permeabilities and static tortuosities (which may compensate for the lack of correction of inertial tortuosity). There is, however, some clear underestimation in sound absorption for the arrangements with small air cavities (see Figure 13).

All cavity resonances are very well predicted by the modelling. A small increase in the frequency which appears in Figures 13–15 around 1.8 kHz was not stable, that is, it could have been even smaller (or a bit larger) depending on how the sample was mounted into the tube.

5 Controlling sound absorption of micro-slotted plates backed by air cavities

The modelling of sound absorption of perforated plates backed with cavities presented in this paper should form a base for development of advanced techniques for optimisation of perforation patterns. In this Section a simple technique for specifying the optimal slit width (or plate thickness, or perforation rate) which maximise the sound absorption of a micro-slotted plate backed by an air cavity will be discussed.

Similarly to plates with circular perforations [5], the sound absorption of micro-slotted plates can be controlled by the plate

thickness ℓ_p, the perforation rate ϕ, and the width of slits a. For a thin perforated plate backed by an air cavity, the surface impedance can be approximated as

$$Z_s(\omega) \approx \sigma_p\,\ell_p + Z_b(\omega)\,, \tag{17}$$

where σ_p is the airflow resistivity related to the perforation, while $Z_b(\omega) = -\mathrm{i}\,Z_f/\tan\left(\omega\ell_c/c_f\right)$ is the backing impedance of air cavity of depth ℓ_c (moreover, here: Z_f and c_f are the characteristic impedance and speed of sound of air, respectively). As demonstrated in [5], a specific (optimal) sound absorption is reached when the specific airflow resistance of plate $\sigma_p\,\ell_p$ equals to the impedance of air Z_f. Using this condition, i.e., $\sigma_p\,\ell_p = Z_f$, and also the formula for airflow resistivity $\sigma_p = \mu_f/k_0$ (where μ_f is the dynamic viscosity of air, while k_0 is the viscous permeability of perforated plate), the following requirement is specified

$$\frac{\ell_p}{k_0} = \frac{Z_f}{\mu_f}\,, \tag{18}$$

which relates the geometric properties of perforated plate (on the left-hand side of this equality) to the physical properties of air (on the right-hand side). The viscous permeability k_0 can be precisely determined for complex perforation patterns from numerical calculations (see Appendix C). On the other hand, for simple perforations (e.g., slits) it can be estimated using formula (16) with the appropriately determined denominator $\mathcal{D}$ (see Figure 10). By applying the estimation (16), the condition (18) can be expressed in the following form

$$\frac{\mathcal{D}\,\ell_p}{\phi\,R_h^2} = \frac{Z_f}{\mu_f}\,, \tag{19}$$

which means that, for example, the hydraulic radius R_h can be adjusted to a specific value

$$R_{h(sp)} = \sqrt{\frac{\mathcal{D}\,\ell_p}{\phi}\,\frac{\mu_f}{Z_f}} \tag{20}$$

which maximises the sound absorption. Note that the optimising condition (19) does not depend on the cavity depth ℓ_c. However, the cavity depth can be used to control the frequency of the maximum sound absorption peak.

For simple perforations the specific airflow resistance, and consequently, the optimising condition (19) depend on three well-defined parameters related to the size of plate and perforation, namely: the plate thickness ℓ_p, the perforation rate ϕ and the hydraulic radius R_h. In an optimal design process one can alternatively fix two of these parameters, and adjust the third one.

As an example, a slit-width optimisation will be proposed here for the micro-slotted plate discussed in Section 3. Using the original plate thickness $\ell_p = 4\,\text{mm}$ and perforation rate $\phi = 7.667\,\%$, and assuming the slit perforation shape as for very long (narrow) slits, i.e., $\mathcal{D} = 12$, the specific slit width $a_{(sp)}$, which is then approximately equal to the specific hydraulic radius, can be estimated thanks to formula (20) as: $a_{(sp)} \approx R_{h(sp)} \approx 0.165\,\text{mm}$.

Figure 19 compares the sound absorption for the original square plate – investigated in Section 3 for two cases of backing cavity (i.e., with the cavity depths of 30 mm and 53 mm) – with the results found for the proposed optimisation. The proposed specific (optimised) slit width of 0.165 mm is smaller than the original value of 0.3 mm. Since this optimised value is found with the assumption that the original perforation rate $\phi = 7.667\,\%$ is preserved,

the number of slits forming the optimised pattern (or, simply, their total length) must be increased to maintain the same perforation rate ϕ.
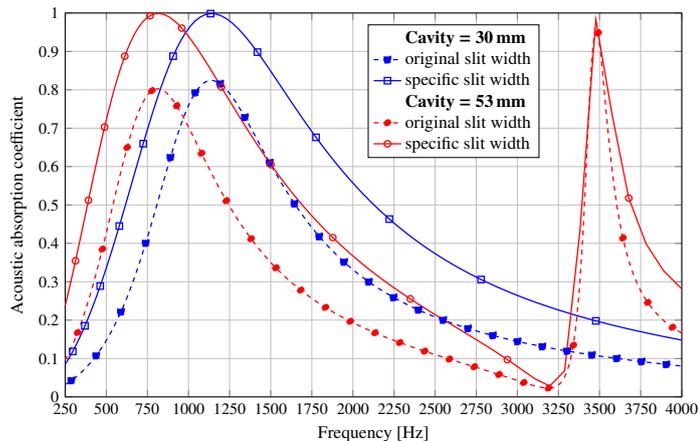

Figure 19: Acoustic absorption for the square micro-slotted plate (with $\ell_\mathrm{p} = 4\,\mathrm{mm}$ and $\phi = 7.667\,\%$) backed with air cavities (30 mm or 53 mm thick) for the original slit width $a = 0.3\,\mathrm{mm}$ and the specific (optimised) value $a_{(\mathrm{sp})} = 0.165\,\mathrm{mm}$ (maintaining, however, the same perforation rate ϕ)

6   Final remarks

For micro-perforated plates and other porous structures with straight (i.e., *not* tortuous) flat-walled slits or channels, the thermal transport parameters are identical with their viscous counterparts, namely: $k_0' = k_0$, $\alpha_0' = \alpha_0$, and $\Lambda' = \Lambda$. It was formally demonstrated that the numerical computations can be then limited to only one 2D finite element analysis, namely, the (thermal) Poisson problem, to find necessary values for $k_0 = k_0'$ and $\alpha_0 = \alpha_0'$ (since $\alpha_\infty = 1$, while ϕ and $\Lambda = \Lambda'$ are determined directly from the micro-geometry). This analysis is purely two-dimensional and it is *not* computationally demanding (compared to the Stokes or Laplace problems). On the other hand, although straight channels (slits) parallel to the flow are not tortuous (i.e., $\alpha_\infty = 1$), the flow bends close to the plate surfaces just outside of the slits (if they are loosely set as they usually are in standard perforated plates), which suggests a correction for tortuosity, namely: $\alpha_\infty > 1$, especially for very thin plates. For thick structures, this correction should rather be local, i.e., on the structure's surface, which may suggest to introduce in this place an additional thin layer of equivalent medium with the corrected tortuosity. Finally, in case of plates with perforations localised in meso-scale areas (like in the disc-shape plate), they can be treated as mesoscopic porous inclusions in a solid matrix of plate [50]. Then, a composite model of a (heterogenous) plate with large mesoscopic pores filled with an equivalent fluid resulting from the localised micro-perforations can be applied [50].

It is assumed that for a given micro-geometry the numerical computations provide accurate values for the permeabilities (k_0' and k_0) and static tortuosities (α_0 and α_0'). Often, the permeabilities can be quite well estimated by the adequate formulas depending on the porosity ϕ and hydraulic radius R_h, namely: $\phi R_\mathrm{h}^2/\mathcal{D}$, where $\mathcal{D} = 12$ for narrow slits, while $\mathcal{D} \approx 8$ for other perforations (ideally and exactly for circular ones); roughly speaking,

for wider (i.e., rectangular) slits $\mathcal{D} \approx 8$ also tends to be more correct. The analytical estimations for static tortuosities result solely from the assumption of the JCA or JCAL models instead of the JCAPL one (see Appendix A), and it is demonstrated that they may significantly differ from their numerically-determined counterparts.

The cavity resonances are very well predicted. They are localised around some particular frequencies higher than the first, i.e., the lowest-frequency peak in sound absorption which is attenuated but spans a much wider frequency range; it is related to the micro-perforations. Typically, the correction of tortuosity slightly increases the lowest-frequency peak and shifts it but only by a hundred of hertz (or less) to some lower frequency. Nevertheless, the effect of small improvements/modifications in modelling can often be blurred by discrepancies coming from measurements. This is especially true when common 3D-printing technologies are used to manufacture prototypes or validation samples. One must be aware of many imperfections which are involved and usually tend to increase the overall sound absorption. Surface roughness, *not* designed micro-pores and fibres, and other imperfections are very common in 3D-printed samples. Moreover, the actual sizes of the designed slits, pores or perforations (crucial for viscous and thermal transport, and so for the overall sound absorption) may slightly but significantly differ from their original designed values. Therefore, the designed micro-geometry must be updated (basing on some examination of the actual samples), before using it for any microstructural calculations. Finally, for large air cavities backing micro-porous plates there is usually a non-negligible increase in absorption (larger at higher frequencies) coming from the dissipation effects on the walls of impedance tube. This also must be somehow compensated: in modelling or by slightly correcting the experimental curves (for example, by using the measurements carried out for the empty tube, i.e., for air cavities without the plate).

Complex perforation patterns can be proposed, especially, when there is more than one objective (i.e., *not only* the one directly related to efficient rigid MPPs and MSAs for air-borne waves). A good example is here a metamaterial plate with small elastic resonators which should eventually be modelled as poroelastic structure in order to take into account the effects of local resonators. On the other hand, the transport parameters and dynamic tortuosities are required, for example, by the Biot-JCAPL poroelastic model and – as demonstrated in the paper – they often should be computed from more accurate numerical analyses instead of the well-known analytical estimations. Such an approach using the Biot-JCAPL model (at the macro-scale level) with accurately-determined transport parameters can be recommended, although the micro-scale-based estimations of dynamic tortuosities are done with the assumption that the solid part of microstructure is motionless. Finally, the ways of modelling compared in the paper should allow for a proper choice between various competing designs, and eventually, should form a base for a more elaborate (shape, topological) techniques for optimisation of perforation patterns.

Acknowledgements

A Formulas for the dynamic tortuosity functions according to JCAPL, JCAL, and JCA models

The dynamic viscous tortuosity function is dimensionless and complex-valued; it can be computed as follows (here, i is the imaginary unit):

$$\alpha(\omega) = \alpha_\infty \left[1 + \frac{\mathcal{F}(\omega)}{\mathrm{i}\widetilde{\omega}} \right], \quad \text{where} \quad \mathcal{F}(\omega) = 1 - \mathcal{P} + \sqrt{\mathcal{P}^2 + \frac{\mathcal{M}}{2}\mathrm{i}\widetilde{\omega}}. \tag{A.1}$$

A dimensionless frequency $\widetilde{\omega}$ for viscous effects (normalised with respect to the kinematic viscosity of pore-fluid ν_f) is introduced here, namely:

$$\widetilde{\omega} = \omega \frac{\alpha_\infty k_0}{\phi \nu_\mathrm{f}}, \tag{A.2}$$

and the viscous pore-shape factor $\mathcal{M}$ and low-frequency viscous correction parameter $\mathcal{P}$ are defined as:

$$\mathcal{M} = \frac{8\alpha_\infty k_0}{\phi \Lambda^2}, \qquad \mathcal{P} = \frac{\mathcal{M}}{4(\alpha_0/\alpha_\infty - 1)}. \tag{A.3}$$

The formula for $\mathcal{P}$ depends on α_0, which is required by the JCAPL model. For JCA and JCAL models $\mathcal{P} = 1$, which is also obtained when α_0 is defined as (B.2).

The dynamic thermal tortuosity is a dimensionless and complex-valued function of frequency and can be computed as follows:

$$\alpha'(\omega) = 1 + \frac{\mathcal{F}'(\omega)}{\mathrm{i}\widetilde{\omega}'}, \quad \text{where} \quad \mathcal{F}'(\omega) = 1 - \mathcal{P}' + \sqrt{\mathcal{P}'^2 + \frac{\mathcal{M}'}{2}\mathrm{i}\widetilde{\omega}'} \tag{A.4}$$

Here, a dimensionless frequency $\widetilde{\omega}'$ for thermal effects is introduced (normalised with respect to $\nu_\mathrm{f}' = \nu_\mathrm{f}/N_\mathrm{f}$, where ν_f and N_f are the kinematic viscosity and Prandtl number for pore-fluid, respectively):

$$\widetilde{\omega}' = \omega \frac{k_0'}{\phi \nu_\mathrm{f}'}, \tag{A.5}$$

and the thermal pore-shape factor $\mathcal{M}'$ and low-frequency thermal correction parameter $\mathcal{P}'$ are defined as:

$$\mathcal{M}' = \frac{8k_0'}{\phi \Lambda'^2}, \qquad \mathcal{P}' = \frac{\mathcal{M}'}{4(\alpha_0' - 1)}. \tag{A.6}$$

The formula for $\mathcal{P}'$ depends on α_0', which is required by the JCAPL model. For JCA and JCAL models $\mathcal{P}' = 1$, which is also obtained for α_0' defined by the formula in (B.3). Moreover, in the original JCA version also $\mathcal{M}' = 1$, which is when k_0' is defined as (B.1).

B Transitions between the semi-phenomenological models

Transitions between JCA and the enhanced models (JCAL and JCAPL) are possible, since analytical formulas can be easily derived for 3 transport parameters which are missing in the JCA case. It is done by comparing the original JCA model and its enhanced versions. The derived formulas require only (some of) the 5 original parameters of JCA model, namely:

- knowing ϕ and Λ', the thermal permeability can be approximated as:

$$k_0' = \frac{\phi \Lambda'^2}{8}; \tag{B.1}$$

- knowing ϕ, α_∞, k_0 and Λ, the viscous static tortuosity can be estimated as:

$$\alpha_0 = \alpha_\infty \left(1 + \frac{2 k_0 \alpha_\infty}{\phi \Lambda^2} \right); \tag{B.2}$$

- finally, knowing ϕ, k_0' and Λ', the following formula can be used for the thermal static tortuosity:

$$\alpha_0' = 1 + \frac{2 k_0'}{\phi \Lambda'^2}, \tag{B.3}$$

and moreover: $\alpha_0' = \frac{5}{4}$, if the thermal permeability k_0' is determined using formula (B.1).

The above formulas formulas – or, as a matter of fact, the original JCA model – are very useful regarding the fact of rather problematic measurability of these parameters. Nevertheless, they can be treated only as some estimations for three additional transport parameters which are not present in the original JCA model (or, for two static tortuosities in the JCAL case). It means that when only 5 parameters of JCA model are known (or 6 as in the JCAL case), an implementation of JCAPL model can still be used provided that it is complemented by these (often very rough) approximations of missing parameters.

On the other hand, there is also an analytical estimation of the viscous characteristic length (useful, especially, for perforated plates) when the well-known and directly measurable parameters of porosity ϕ, (viscous) permeability k_0, and tortuosity α_∞ are known; then:

$$\Lambda \approx \sqrt{\frac{8 \alpha_\infty k_0}{\phi}}. \tag{B.4}$$

In that way, the 5-parameter JCA model can be reduced to a 4-parameter model. However, this approximation is valid for round (ideally, circular) perforations, so for perforations of more complex shapes (or, e.g., for slits) this would be a very rough and often unacceptable estimation. Notice also that a similar relation between the thermal length and thermal permeability (i.e., $\Lambda' \approx \sqrt{8k_0'/\phi}$) appears in the formula (B.1), which again suggests the assumption of circular perforations.

C Permeability and static tortuosity – numerical calculations from microstructure

The viscous permeability parameter k_0 can be numerically determined by solving the Stokes' flow problem describing a viscous incompressible flow through a representative periodic fluid domain Ω (set on open-porosity ϕ) with no-slip boundary conditions on solid walls $\partial_s \Omega$. The flow is caused by a uniform (i.e., constant over the whole domain Ω) vector field of macroscopic pressure gradient in some specified direction of macroscopic flow. The Stokes equations can be re-scaled, so that the macroscopic pressure gradient is a dimensionless unit vector field $\underline{e}$, and in that case the local field of flow velocity is normalised to the vector field $\underline{k}$ with the dimension of permeability [m^2], whereas the local pressure field is normalised to the local field q with the dimension [m]. Such re-scaled Stokes' equations are as follows:

$$-\nabla^2 \underline{k} + \nabla q = \underline{e}, \quad \nabla \cdot \underline{k} = 0 \quad \text{in} \quad \Omega, \qquad \text{(C.1)}$$

with the homogeneous (no-slip) boundary conditions to be satisfied on solid walls

$$\underline{k} = \underline{0} \quad \text{on} \quad \partial_s \Omega, \qquad \text{(C.2)}$$

and the periodic conditions for $\underline{k}$ on the relevant faces of periodicity $\partial_p \Omega$. When the vector field $\underline{k}$ is found, it can be averaged over the flow domain Ω, multiplied by the porosity ϕ and projected onto the macroscopic pressure gradient direction $\underline{e}$ to determine the permeability in that direction, namely:

$$k_0 = \phi \langle \underline{k} \rangle_\Omega \cdot \underline{e} = \phi \langle \underline{k} \cdot \underline{e} \rangle_\Omega = \frac{\phi}{\Omega} \int\limits_\Omega \underline{k} \cdot \underline{e}\, \mathrm{d}V. \qquad \text{(C.3)}$$

In case of flows in the x_3-direction through flat-walled channels or slits (with all channel walls in parallel to the direction of flow) set in any pattern on the (x_1, x_2)-plane, there is no change along the x_3-coordinate and the following mathematical relations are met:

$$\frac{\partial}{\partial x_3} \equiv 0, \qquad \underline{k} = \begin{bmatrix} k_1 \\ k_2 \\ k_3 \end{bmatrix} = \begin{bmatrix} 0 \\ 0 \\ k_3(x_1, x_2) \end{bmatrix},$$
$$q = q(x_1, x_2), \qquad \underline{e} = \begin{bmatrix} e_1 \\ e_2 \\ e_3 \end{bmatrix} = \begin{bmatrix} 0 \\ 0 \\ 1 \end{bmatrix}. \qquad \text{(C.4)}$$

Using these relations for the first equation of the normalised Stokes flow (C.1) yields the following two-dimensional equations (defined in A_Ω, which denotes the cross-section of Ω)

$$\frac{\partial q}{\partial x_1} = 0, \qquad \frac{\partial q}{\partial x_2} = 0, \qquad \text{(C.5)}$$

$$-\left(\frac{\partial^2 k_3}{\partial x_1^2} + \frac{\partial^2 k_3}{\partial x_2^2} \right) = 1 \quad \text{in} \quad A_\Omega, \qquad \text{(C.6)}$$

with the corresponding homogeneous condition $k_3 = 0$ defined on the solid boundary $\partial_s A_\Omega$ of the cross-section, and the periodic condition for k_3 on the relevant edges of periodicity $\partial_p A_\Omega$ (if they exist). Equation (C.6) appears to be the Poisson problem in the (x_1, x_2)-plane. Equations (C.5) show that q must be

constant, which is anyway irrelevant, since q is a balance field, not used in averaging when the macroscopic transport parameter of permeability is determined. Moreover, since $k_1 = k_2 = 0$ and $\frac{\partial}{\partial x_3} = 0$, the incompressibility condition is identically met, namely, $\nabla \cdot \underline{k} = \frac{\partial k_1}{\partial x_1} + \frac{\partial k_2}{\partial x_2} + \frac{\partial k_3}{\partial x_3} \equiv 0$. Therefore, the normalised velocity field $k_3(x_1, x_2)$ is simply computed as the solution of the two-dimensional Poisson problem (C.6). When this normalised field is found the macroscopic parameter of viscous permeability k_0 (in the direction of flow) is determined by averaging this field over the whole cross section area A_Ω and multiplying the result by the porosity ϕ, namely:

$$k_0 = \phi \langle k_3 \rangle_{A_\Omega} = \frac{\phi}{A_\Omega} \int\limits_{A_\Omega} k_3(x_1, x_2)\, \mathrm{d}S. \qquad \text{(C.7)}$$

In general, the thermal permeability k_0' is found by averaging (over the periodic fluid domain Ω) the local field k' (which can be treated as a field of temperature normalised to the dimension of permeability [m^2]) found as a solution of the Poisson problem (related to a thermal diffusion in Ω caused by a uniform source normalised to a dimensionless unit field):

$$-\nabla^2 k' = 1 \quad \text{in} \quad \Omega, \qquad \text{(C.8)}$$

with the homogeneous (isothermal) boundary condition $k' = 0$ on solid walls $\partial_s \Omega$, and the periodic conditions for k' on the relevant faces of periodicity $\partial_p \Omega$. In case of thermal transport inside flat-walled channels: $\frac{\partial}{\partial x_3} \equiv 0$ and $k' = k'(x_1, x_2)$, and equation (C.8) reduces to its two-dimensional form defined on the cross-section A_Ω, namely,

$$-\left(\frac{\partial^2 k'}{\partial x_1^2} + \frac{\partial^2 k'}{\partial x_2^2} \right) = 1 \quad \text{in} \quad A_\Omega, \qquad \text{(C.9)}$$

with the homogeneous condition $k' = 0$ on the cross-section boundary $\partial_s A_\Omega$, and the periodic condition for k' on the relevant edges of periodicity $\partial_p A_\Omega$ (if they exist). The macroscopic parameter of thermal permeability is computed as an average of the filed k' over the cross-section A_Ω multiplied by the porosity ϕ:

$$k_0' = \phi \langle k' \rangle_{A_\Omega} = \frac{\phi}{A_\Omega} \int\limits_{A_\Omega} k'(x_1, x_2)\, \mathrm{d}S. \qquad \text{(C.10)}$$

Since the two Poisson problems (C.6) and (C.9) are identical, their solutions are the same, namely, $k_3(x_1, x_2) = k'(x_1, x_2)$, and so are the macroscopic permeabilities: $k_0 = k_0'$. Finally, also the static tortuosities (the viscous one and thermal one) are identical:

$$\alpha_0 = \alpha_0' = \frac{\langle k'^2 \rangle_{A_\Omega}}{\langle k' \rangle_{A_\Omega}^2}. \qquad \text{(C.11)}$$

D Tortuosity and characteristic lengths – numerical calculations from microstructure

At very high frequency, the flows through porous media tend to be purely inertial (i.e., the viscosity of fluid can be neglected). Such perfect (i.e., inviscid and incompressible) flows formally coincide

14

with an electrical problem of a dielectric porous material filled with a conductive fluid. The effective electric conductivity of such a composite is related to the tortuosity of its open pore space Ω. The (inertial) tortuosity parameter (and also the viscous characteristic length) can be determined from the solution of a re-scaled electric problem for the normalised (dimensionless) electric field $\underline{E}$:

$$\underline{E} = \underline{e} - \nabla\tilde{q}, \quad \nabla \cdot \underline{E} = 0 \quad \text{in} \quad \Omega, \qquad \text{(D.1)}$$

where $\tilde{q}$ is the consistently normalised (to the dimension [m]) local field of electric potential, and $\underline{e}$ is the normalised (dimensionless) unit external (global) electric field uniform in the whole fluid domain Ω, which induces the local field $\underline{E}$. The following boundary conditions must be satisfied on the dielectric solid walls:

$$\underline{E} \cdot \underline{n} = 0 \quad \text{on} \quad \partial_s\Omega, \qquad \text{(D.2)}$$

while the periodic conditions for $\underline{E}$ and $\tilde{q}$ are set on the relevant faces of periodicity $\partial_p\Omega$. This problem reduces to the Laplace equation

$$\nabla^2\tilde{q} = 0 \quad \text{in} \quad \Omega, \qquad \text{(D.3)}$$

with the boundary condition

$$\nabla\tilde{q} \cdot \underline{n} = \underline{e} \cdot \underline{n} \quad \text{on} \quad \partial_s\Omega, \qquad \text{(D.4)}$$

and the periodic conditions for $\tilde{q}$ on the relevant faces of periodicity $\partial_p\Omega$. When the Laplace problem is solved and $\underline{E}$ is computed from the first equation of (D.1), the (inertial) tortuosity parameter can be determined from the following formula

$$\alpha_\infty^{-1} = \langle \underline{E} \cdot \underline{e} \rangle_\Omega, \qquad \text{(D.5)}$$

whereas the viscous and thermal characteristic lengths are computed as follows

$$\Lambda = 2\frac{\int_\Omega \underline{E} \cdot \underline{E}\,\mathrm{d}V}{\int_{\partial_s\Omega} \underline{E} \cdot \underline{E}\,\mathrm{d}S}, \qquad \Lambda' = 2\frac{\int_\Omega \mathrm{d}V}{\int_{\partial_s\Omega} \mathrm{d}S}. \qquad \text{(D.6)}$$

Notice again that the thermal length Λ' depends purely on geometry: it is defined as a doubled ratio of fluid domain to the total surface of solid walls, which can be seen as a generalisation of the so-called hydraulic radius (which is introduced in Section 2.3).

In case of parallel flat-walled channels in the x_3-direction and with $\underline{e}$ set in that direction:

$$\frac{\partial}{\partial x_3} \equiv 0, \qquad \underline{E} = \begin{bmatrix} E_1 \\ E_2 \\ E_3 \end{bmatrix} = \begin{bmatrix} 0 \\ 0 \\ E_3(x_1,x_2) \end{bmatrix},$$

$$\tilde{q} = \tilde{q}(x_1,x_2), \qquad \underline{e} = \begin{bmatrix} e_1 \\ e_2 \\ e_3 \end{bmatrix} = \begin{bmatrix} 0 \\ 0 \\ 1 \end{bmatrix}. \qquad \text{(D.7)}$$

Then, the potential $\tilde{q}$ becomes constant since the first equation in (D.1) reduces to

$$0 \equiv E_1 = -\frac{\partial\tilde{q}}{\partial x_1}, \qquad 0 \equiv E_2 = -\frac{\partial\tilde{q}}{\partial x_2}, \qquad E_3 = 1. \quad \text{(D.8)}$$

Moreover, in that case: $\underline{E} \cdot \underline{e} = 1$ and $\underline{E} \cdot \underline{E} = 1$, which means that (as expected) $\alpha_\infty = 1$, and the characteristic lengths are equal and can be computed as the doubled ratio of cross-section area A_Ω to

the total length of its solid boundaries (see the definitions of wetted perimeter and hydraulic radius in Section 2.3):

$$\Lambda = \Lambda' = 2\frac{\int_{A_\Omega} \mathrm{d}S}{\int_{\partial_s A_\Omega} \mathrm{d}L}. \qquad \text{(D.9)}$$

All that means that the tortuosity and characteristic lengths are determined solely by the micro-geometry.

References

[1] S.-H. Park, A design method of micro-perforated panel absorber at high sound pressure environment in launcher fairings. *J. Sound Vib.* 332 (2013) 521–531.

[2] S.-H. Park, Acoustic properties of micro-perforated panel absorbers backed by Helmholtz resonators for the improvement of low-frequency sound absorption. *J. Sound Vib.* 332 (2013) 4895–4911.

[3] H. Ruiz, P. Cobo, F. Jacobsen, Optimization of multiple-layer microperforated panels by simulated annealing. *Appl. Acoust.* 72 (2002) 772–776.

[4] F. C. Sgard, X. Olny, N. Atalla, F. Castel, On the use of perforations to improve the sound absorption of porous materials. *Appl. Acoust.* 66 (2005) 625–651.

[5] F. Chevillotte, Controlling sound absorption by an upstream resistive layer. *Appl. Acoust.* 73 (2012) 56–60.

[6] J. Carbajo, J. Ramis, L. Godinho, P. Amado-Mendes, Assessment of methods to study the acoustic properties of heterogeneous perforated panel absorbers. *Appl. Acoust.* 133 (2018) 1–7.

[7] M. J. Swift, K. V. Horoshenkov, P. Leclaire, D. C. Hothersall, K. Fujiwara, H. Torihama, On the effect of the bending vibration on the acoustic properties of thin poroelastic plates. *J. Acoust. Soc. Am.* 107 (2000) 1786–1789.

[8] H. Aygun, K. Attenborough, The insertion loss of perforated porous plates in a duct without and with mean air flow. *Appl. Acoust.* 69 (2008) 506–513.

[9] H. Aygun, K. Attenborough, Sound absorption by clamped poroelastic plates. J. Acoust. Soc. Am. 134 (2008) 1550–1556.

[10] D.-Y. Maa, Potential of microperforated panel absorber. *J. Acoust. Soc. Am.* 104 (1998) 2861–2866.

[11] R. Tayong, T. Dupont, P. Leclaire, Experimental investigation of holes interaction effect on the sound absorption coefficient of micro-perforated panels under high and medium sound levels. *Appl. Acoust.* 72 (2011) 777-784.

[12] J. F. Allard, *Propagation of Sound in Porous Media. Modelling Sound Absorbing Materials*. Elsevier, 1993.

[13] U. R. Kristiansen, T. E. Vigran, On the design of resonant absorbers using a slotted plate. *Appl. Acoust.* 43 (1994) 39–48.

[14] D.-Y. Maa, Theory of microslit absorbers. *Chinese J. Acoust.* 20 (2001) 1–10.

[15] R. T. Randeberg, Adjustable slitted panel absorber. *Acta Acust. united Ac.* 88 (2002) 507–512.

[16] K. Attenborough, Acoustical characteristics of porous materials, *Phys. Rep.* 82 (1982) 179–227.

[17] N. Atalla, F. Sgard, Modeling of perforated plates and screens using rigid frame porous models. *J. Sound Vib.* 303 (2007) 195–208.

[18] J. Wang, P. Rubini, Q. Qin, Application of a porous media model for the acoustic damping of perforated plate absorbers. *Appl. Acoust.* 127 (2017) 324–335.

[19] J. F. Allard, N. Atalla, *Propagation of Sound in Porous Media: Modelling Sound Absorbing Materials, Second Edition*. Wiley, 2009.

[20] U. Ingard, On the theory and design of acoustic resonators. *J. Acoust. Soc. Am.* 25 (1953) 1037–1061.

[21] M. R. Stinson, Y. Champoux, Propagation of sound and the assignment of shape factors in model porous materials having simple pore geometries. *J. Acoust. Soc. Am.* 91 (1992) 685–695.

[22] J. F. Ning, S. W. Ren, G. P. Zhao, Acoustic properties of micro-perforated panel absorber having arbitrary cross-sectional perforations. *Appl. Acoust.* 111 (2016) 135–142.

[23] L. Jaouen, F. Chevillotte, Length correction of 2D discontinuities or perforations at large wavelengths and for linear acoustics. *Acta Acust. united Ac.* 104 (2018) 243–250.

[24] T. G. Zieliński, Pore-size effects in sound absorbing foams with periodic microstructure: modelling and experimental verification using 3D printed specimens, in: P. Sas, D. Moens, A. van de Walle (Eds.), *Proceedings of ISMA2016 International Conference on Noise and Vibration Engineering and USD2016 International Conference on Uncertainty in Structural Dynamics*, KU Leuven (Belgium), 2016, pp.95–104.

[25] K. Attenborough, Microstructures for lowering the quarter wavelength resonance frequency of a hard-backed rigid-porous layer. *Appl. Acoust.* 130 (2018) 188–194.

[26] D. L. Johnson, J. Koplik, R. Dashen, Theory of dynamic permeability and tortuosity in fluid-saturated porous media. *J. Fluid Mech.* 176 (1987) 379–402.

[27] Y. Champoux, J.-F. Allard, Dynamic tortuosity and bulk modulus in air-saturated porous media. *J. Appl. Phys.* 70 (1991) 1975–1979.

[28] S. R. Pride, F. D. Morgan, A. F. Gangi, Drag forces of porous-medium acoustics, *Phys. Rev. B* 47 (1993) 4964–4978.

[29] D. Lafarge, *Propagation du son dans les matériaux poreux à structure rigide saturés par un fluide viscothermique.* (Sound propagation in porous materials with rigid frame saturated by a visco-thermal fluid.) Ph.D. dissertation (in French), Université du Maine (France), 1993.

[30] D. Lafarge, P. Lemarinier, J. F. Allard, V. Tarnow, Dynamic compressibility of air in porous structures at audible frequencies, *J. Acoust. Soc. Am.* 102 (1997) 1995–2006.

[31] D. Lafarge, The equivalent fluid model. Chapt. 6 (pp. 167–201) in: *Materials and Acoustics Handbook*, ISTE, Wiley, 2009.

[32] APMR – Acoustical Porous Material Recipes, http://apmr.matelys.com/ (date last viewed 22/05/2018).

[33] S. Gasser, F. Paun, and Y. Bréchet, Absorptive properties of rigid porous media: Application to face centered cubic sphere packing. *J. Acoust. Soc. Am.* 117 (2005), 2090–2099.

[34] Ch.-Y. Lee, M. J. Leamy, J. H. Nadler, Acoustic absorption calculation in irreducible porous media: A unified computational approach. *J. Acoust. Soc. Am.* 126 (2009) 1862–1870.

[35] T. G. Zieliński, Microstructure-based calculations and experimental results for sound absorbing porous layers of randomly packed rigid spherical beads. *J. Appl. Phys.* 116 (2014) 034905.

[36] C. Perrot, F. Chevillotte, and R. Panneton, Bottom-up approach for microstructure optimization of sound absorbing materials. *J. Acoust. Soc. Am.* 124 (2008), 940–948.

[37] C. Perrot, R. Panneton, and X. Olny, Periodic unit cell reconstruction of porous media: Application to open-cell aluminum foams. *J. Appl. Phys.* 101 (2007) 113538.

[38] C. Perrot, F. Chevillotte, and R. Panneton, Dynamic viscous permeability of an open-cell aluminum foam: Computations versus experiments. *J. Appl. Phys.* 103 (2008) 024909.

[39] C. Perrot, F. Chevillotte, M. T. Hoang, G. Bonnet, F.-X. Bécot, L. Gautron, and A. Duval, Microstructure, transport, and acoustic properties of open-cell foam samples. Experiments and three-dimensional numerical simulations. *J. Appl. Phys.* 111 (2012) 014911.

[40] T. G. Zieliński, Generation of random microstructures and prediction of sound velocity and absorption for open foams with spherical pores. *J. Acoust. Soc. Am.* 137 (2015) 1790–1801.

[41] F. Chevillotte, C. Perrot, and E. Guillon, A direct link between microstructure and acoustical macro-behavior of real double porosity foams. *J. Acoust. Soc. Am.* 134 (2013), 4681–4690.

[42] T. G. Zieliński, Microstructure representations for sound absorbing fibrous media: 3D and 2D multiscale modelling and experiments. *J. Sound Vib.* 409 (2017) 112–130.

[43] H. T. Luu, C. Perrot, R. Panneton, Influence of porosity, fiber radius and fiber orientation on the transport and acoustic properties of random fiber structures. *Acta Acust. united Ac.* 103 (2017) 1050–1063.

[44] https://en.wikipedia.org/wiki/ Manning_formula#Hydraulic_radius (date last viewed 22/05/2018).

[45] https://en.wikipedia.org/wiki/Hydraulic_diameter (date last viewed 22/05/2018).

[46] L. L. Beranek, I. L. Ver, *Noise and Vibration Control Engineering*. Wiley, New York, 1992.

[47] B. Brouard, D. Lafarge, J.-F. Allard, A general method of modelling sound propagation in layered media. *J. Sound Vib.* 114 (1987) 565–581.

[48] T. G. Zieliński, Normalized inverse characterization of sound absorbing rigid porous media, *J. Acoust. Soc. Am.* 137 (2015) 3232–3243.

[49] H. Ruiz, C. Claeys, E. Deckers, W. Desmet, Numerical and experimental study of the effect of microslits on the normal absorption of structural metamaterials. *Mech. Syst. Sig. Process.* 70 (2016) 904–918.

[50] F. Chevillotte, L. Jaouen, F.-X. Bécot, On the modeling of visco-thermal dissipations in heterogeneous porous media. *J. Acoust. Soc. Am.* 138 (2015) 3922–3929.